Unravelling ultrafast Li-ion transport in functionalized metal-organic-framework based battery electrolytes

Guorui Cai[1,†], Amanda A. Chen[1,†], Sharon Lin[2], Dong Ju Lee[1], Kunpeng Yu[1], John Holoubek[1], Yijie Yin[3], Anthony U. Mu[1], Ying Shirley Meng[1,4], Ping Liu[1,2,3,5], Seth M. Cohen[1,2,], Tod A. Pascal[1,2,3,5,*] and Zheng Chen[1,2,3,5,*]*

[1]Department of Nano and Chemical Engineering, University of California, San Diego, La Jolla, CA 92093, USA

[2]Department of Chemistry and Biochemistry, University of California, San Diego, La Jolla, CA 92093, USA

[3]Program of Materials Science and Engineering, University of California, San Diego, La Jolla, CA 92093, USA

[4]Pritzker School of Molecular Engineering, University of Chicago, Chicago, IL, 60637, USA

[5]Sustainable Power and Energy Center, University of California, San Diego, La Jolla, CA 92093, USA

[†]These authors contributed equally to this work.

[*]Correspondence to: zhengchen@eng.ucsd.edu; tpascal@ucsd.edu; scohen@ucsd.edu

This PDF file includes supplementary experimental methods and computational details, tables S1-S4, and figures S1-S17.

Other supplementary information for this manuscript includes videos S1 and S2.

Supplementary Methods

1. Experimental Details

1.1 Preparation of metal-organic frameworks (MOFs)

N, N-dimethylformamide (DMF), acetic acid, and methanol were purchased from Fisher Scientific and used as received. Zirconium chloride ($ZrCl_4$) was purchased from Strem and stored in a desiccator prior to use. Terephthalic acid (H_2bdc), 2-aminoterephthalic acid (H_2bdc-NH_2), and 2-nitroterephthalic acid (H_2bdc-NO_2) were purchased from Sigma-Aldrich and used as received. A metal salt solution was prepared by adding $ZrCl_4$ (2.62 mmol, 0.611 g) and $N,$ N-dimethylformamide (DMF, 50 mL) into a Teflon-lined reaction vessel (250 mL). Similarly, a ligand solution (50 mL) was prepared in another vessel containing an organic ligand (2.57 mmol). H_2bdc (0.427 g), H_2bdc-NH_2 (0.466 g), and H_2bdc-NO_2 (0.543 g) were used for UiO-66, UiO-66-NH_2, and UiO-66-NO_2, respectively. After being fully dissolved with the aid of sonication (~1 min), the ligand solution was transferred to the metal salt solution. Subsequently, additional DMF (50 mL), acetic acid (29.5 mL), and deionized water (125 μL) were added to the reaction mixture. The reaction vessel was heated at 120 °C in a convection oven for 24 h. After cooling to ambient temperature, MOF powders were collected via centrifugation (7000 RPM, 10 min), washed with 3×20 mL of DMF and 3×20 mL of methanol, and then dried in a vacuum oven at 120 °C overnight.

1.2. Preparation of MOF-polymer mixed-matrix membranes (MMMs)

MOFs were ground into fine powders using a mortar and pestle by hand. A MOF suspension was prepared via sonication (>30 min) of the MOFs in N-methyl-2-pyrrolidone (NMP) solvent. PVDF dissolved in NMP solvent (12 wt%) was then added to the MOF suspension to create a homogeneous MOF/PVDF slurry in NMP solvent with a selected mass ratio, which was then stirred in a Thinky mixer for 30 min and then cast onto a glass substrate. MMM slurry thickness was controlled (100 to 300 μm) via drawdown coating by a doctor blade. The membrane was removed from the glass substrate after drying under a vacuum at 80 °C overnight to produce the final free-standing MMMs. The MMMs were dried under a vacuum oven at 120 °C overnight before use (**Fig. S4**).

1.3. Cathode fabrication

SPAN powders were obtained by annealing a homogeneous mixture of elemental sulfur (S, Sigma-Aldrich) and polyacrylonitrile (PAN, M_w = 150,000) with a mass ratio of 4/1 at 450 °C in an argon-filled tube furnace for 6 h. The prepared SPAN powders, Super-P carbon black, MOFs, and PAA-EA binder with a mass ratio of 7/1.5/0.5/1 were dispersed in NMP via a Thinky mixer. The obtained slurry was cast on a carbon-coated Al foil with a doctor blade to control its thickness. After being dried at 80 °C for 12 h, respectively, the resulting electrodes present a typical SPAN mass loading of ~7.0 mg/cm^2.

1.4. Electrochemical measurements

For Li//Cu coin cells, CR-2032 type coin cells were assembled by using a Li chip (7/16 inch), a larger size Cu disc (18 mm), and selected MMMs or Celgard 2500 as the separator, and 1 M LiFSI in DEE as the electrolytes.

For Li//SPAN pouch cells, the full cells with a low negative-to-positive capacity ratio (N/P ratio ~ 1.4) were assembled with MMM-based composite membranes or Celgard 2500 as the separator, 1 M LiFSI in DEE as the electrolyte, a thin Li chip (50 μm), and a high loading of SPAN cathodes (~4.2 mAh/cm^2 SPAN, 5.7 cm * 4.4 cm). The stacking pressure of pouch cells was controlled at around 100 kPa.

1.5. Material characterization

N$_2$ Gas Sorption Analysis. MOF samples were activated under high vacuum before analysis. ~50 mg of MOF sample was transferred to a pre-weighed sample tube and degassed at 120 °C for 18 h. After degassing, the sample tube containing MOFs was reweighed to obtain a consistent mass for the sample. N$_2$ sorption isotherms were collected on a Micromeritics ASAP 2020 Adsorption Analyzer at 77 K using volumetric techniques, and BET surface areas (m^2/g) were calculated via the Brunauer–Emmett–Teller (BET) method.

Powder X-Ray Diffraction (PXRD). Powder X-ray diffraction (PXRD) patterns of selected MOFs and MMMs were carried out on a Bruker D8 Advance diffractometer by using Cu Kα

radiation. ~50 mg of sample was mounted onto a silicon sample holder, and PXRD patterns were collected at ambient temperature at 40 kV and 40 mA with a scan speed of 0.5 sec/step, a step size of 0.05°, and a 2θ range of 5–50°.

Scanning Electron Microscopy (SEM). The morphologies of selected MMMs and plated Li on copper foils were characterized using an FEI Quanta 250 SEM instrument. Samples were transferred to silicon wafers adhered onto sample holder disks using carbon tape. Prior to analysis, samples were sputter-coated using an Ir sputter coater for 12 s. Images were acquired using a 5 keV energy source with a spot size of 3 under high vacuum at a working distance of 10 mm.

Fourier Transform-Infrared (FT-IR) Spectroscopy. Fourier transform-Infrared (FT-IR) spectra of different MOFs and DEE-soaked MOF powders was collected on a Nicolet 6700 with Smart-iTR diamond ATR crystal using attenuated total reflectance (ATR) mode.

2. Computational Details

2.1 Calculation of the properties of the homogenous systems

2.1.1 Pure DEE density, entropy, and free energy calculations

We optimized the OPLS-AA forcefield[1,2] and slightly modified the epsilon and sigma parameters of the Lennard-Jones potentials in order to minimize differences between the binding energies predicted by the forcefield and calculated by Quantum Mechanical (QM)

electronic structure calculations (**Table S1**). The result was a new set of parameters with 5% smaller epsilon and 15% smaller sigma values. We then used this forcefield to perform equilibrium MD simulations with LAMMPS.[3] We used a numerical integration timestep of 1.0 fs, with a 1 nm van der Waals and real space coulomb cutoff, while the long-range electrostatic were evaluated using a particle-particle particle-mesh solver, with a convergence threshold of 10^{-6}.

A box of 64 DEE molecules (initial density of 0.713 g/cm^3) was constructed by an in-house Perl script and subjected to an initial 500 steps energy minimization using the Conjugate Gradient algorithm. This was followed by 10 ps dynamics in the canonical (constant volume, constant temperature or NVT) ensemble, using a Nose-Hoover thermostat to heat the system slowly from 0–298 K. Afterwards, we performed 2 ns of MD in the Gibbs (isothermal-isobaric or NPT) ensemble, where the temperature was maintained using the Generalized Langevin Equation thermostat[4] with a coupling constant of 0.1 ps, while the system pressure was maintained at 1atm using an Andersen barostat with a coupling constant of 1 ps. This was followed by a further 400 ps of NVT dynamics, saving the trajectory (atomic positions and velocities) every 4 fs. The thermodynamics were calculated from post-trajectory analysis, using an in-house code[5] that implements the Two-Phase Thermodynamic (2PT) method.[6]

2.1.2 Calculating the MOF heat capacity

We described the UiO-66 structure using the UFF[7] forcefield, with charges obtained from charge equilibration,[8] which has been shown to reproduce various properties of UiO-66 in good agreement with experiments.[9] To further validate the forcefield, we calculated the constant pressure heat capacity (C_p) from the enthalpy changes at different temperature ($C_p = \dfrac{dH}{dT}$). We employed a 2x2x2 MOF supercell, with 3648, 4032, and 4032 atoms for UiO-66, UiO-66-NH$_2$, and UiO-66-NO$_2$, respectively. Each MD simulation was initiated with 500 steps of CG minimization, followed by 10 ps NVT simulation to heat to the defined temperature. Afterwards, NPT simulations were used to optimize the volume, followed by 3 ns of NVT simulation. We calculated the average enthalpy from the final 0.2 ns NVT simulation. The calculated C_p of UiO-66 was calculated to be 1.73 kJ/(kg K), in good agreement with a previous study.[10] Within the same computational framework, we calculated slightly larger C_p values for UiO-66-NH$_2$ (1.93 kJ/(kg K)) and UiO-66-NO$_2$ (1.97 kJ/(kg K)).

2.2 Parameterization of MOF|DEE interaction energies from quantum mechanics (QM)

We determined the interaction energies of DEE with representative models of the MOF systems, using Density Functional Theory (DFT) calculations at the PBE/GGA level of theory with Quantum Espresso.[11] Energies were calculated with ultrasoft pseudopotentials and the Grimme-D3 empirical van der Waals corrections,[12] with the kinetic energy cutoff 30 Ry, an electron density cutoff of 150 Ry and (4,4,4) K-Point grid. The model structures for each MOF

system comprised a DEE molecule and a Zr-cluster-linker of a MOF. Four (4) separate DEE orientations were considered, and the interaction energies between MOF and DEE were computed by 5 displacements of the DEE, 0.5Å each, from the MOF structure. The MOF|DEE structures and the corresponding most favorable energy for that configuration were shown in **Table S2**. The interaction parameters between (functionalized) BDC linkers and a DEE molecule were optimized by a nonlinear function optimizer to minimize the difference between the forcefield and QM interaction energies. All other parameters were taken from the **Supplementary Information, Section 2.1** using the arithmetic mixing rule. The optimized parameters and the comparison between QM energies and fitted-forcefield energies were detailed in **Table S3**.

2.3 Grand Canonical Monte Carlo simulation of DEE adsorption capacity inside MOFs

Grand Canonical Monte Carlo (GCMC) simulations, using the MCCCS Towhee code,[13] were used to calculate the DEE loading inside the MOFs.[14] Here, the DEE structure was optimized using QM at the 6-311G*/MP2 level of theory, and the MOFs structures were taken as the final snapshots from our equilibrium MD simulations at 298 K and 1 atm. Each GCMC simulation involved 3 million steps, where the thermodynamics during the last 0.5 million steps were collected and averaged to determine DEE capacities reported in (**Fig. 2d**).

2.4 Evaluating the properties of DEE confined in MOFs

2.4.1   Determining the phase transition point

In our previous work, we demonstrated that confined fluoromethane (FM) experienced a phase transition at a lower pressure than bulk FM by analyzing the translational diffusion coefficient.[14] We adopted a similar strategy here, where we calculated the adsorbate (DEE) translational diffusion coefficient inside the MOFs via MD simulations and the 2PT method. For each system, we used 5 independent, 0.4 ns trajectories (saved every 4 fs) and obtained the self-diffusion constants of DEE using the Green-Kubo method.[15,16] The average value and the standard deviation (**Fig. 2c** and **Fig. S9**) of the confined DEE inside UiO-66-NH$_2$, UiO-66-NO$_2$, and UiO-66 showed a first order phase transition (as determined by a discontinuity in the self-diffusion constant) at 0.0001–0.001 atm, 0.00004–0.0004 atm, and 0.001–0.006 atm, respectively, which were much smaller than the bulk DEE vapor pressure (0.7 atm) at 298 K.[17]

2.4.2 Evaluation of the Helmholtz free energy difference between confined and bulk DEE

We calculated the Helmholtz free energy difference between confined DEE molecules inside the MOFs and a corresponding number of free DEE in the bulk ($\Delta A = A_{confined} - A_{free}$). Here, we obtained the initial DEE|MOF structure from our GCMC simulations and performed the usual equilibrium MD procedure. As before, we took 5 independent 0.4 ns NVT trajectories to calculate the entropy, quantum corrections to the enthalpy, and Helmholtz free energy of

each group of atoms/molecules inside the MOFs. Reference calculations of free DEE, using 1.5ns NVT trajectories, were also performed.

2.4.3 Evaluation of the Helmholtz free energy difference between confined DEE and gas DEE

To determine the Helmholtz free energy of gas DEE, we considered an isolated DEE system with gas density 0.003354 g/cm^3 and proceeded with the internal energy computation for a 1.5 ns NVT trajectory with quantum corrections as before. From the Helmholtz equation, and given that S(gas) = 342.2 J/(mol K)[18], the Helmholtz free energy of gas DEE was then obtained.

2.4.4 Evaluation of the vapor pressures for confined and bulk DEE

We estimated the DEE vapor pressures from Raoult's Law. From the chemical potential equation $\mu = \mu_0 + RT \ln\left(P/P_0\right)$, the vapor pressure difference between confined and bulk DEE, $\dfrac{P_{MOF}^0}{P_{bulk}^0}$, becomes: $\dfrac{P_{MOF}^0}{P_{bulk}^0} = \exp\left(\dfrac{\mu_{MOF} - \mu_{bulk}}{RT}\right)$, where μ_i is the per-molecule Helmholtz energy: $\mu_i = A_i/N$.

2.5 Determining the average Li$^+$ ion solvation structure

We analyzed the coordination number of oxygen atoms (of DEE and FSI$^-$) around a Li$^+$ ion from our equilibrium MD trajectories. Li-FSI parameters were taken from Liu et al.[19] Each MD simulation comprised a 2x2x2 MOF (UiO-66, UiO-66-NH$_2$, and UiO-66-NO$_2$) with the following DEE soaking amount (DEE/MOF wt.%: 11% [UiO-66], 21% [UiO-66-NH$_2$], and

14% [UiO-66-NO$_2$]) and, based on number of DEE molecules, Li-FSI salt in a 1 M concentration. Each system was then simulated using the same procedure as before and the last 2 ns NVT trajectory was used to calculate the coordination numbers, as the integral of the radial distribution functions (**Fig. S12**). The radial distribution functions were shown in **Fig. S13**.

2.6 Free energy surfaces via metadynamics simulations

We quantified the two-dimensional free energy surface of Li$^+$ - MOF side-chain interactions and Li$^+$ solvent coordination by means of accelerated MD simulations and the Metadynamics[20-22] approach. We accelerated convergence by employing the well-tempered formulation,[23] where the bias deposition rate decreases over time by rescaling the heights of the deposited Gaussian functions. We initiated each simulation, from the same structures as detailed in **Supplementary Information, Section 2.5**. To further accelerate the calculations, we confined the Li$^+$ ion inside 1 nm-diameter sphere region, where the center of the sphere was set as the center of the MOF-linker, using a harmonic spring potential. The Metadynamics simulations were performed using two collective variables: 1) the Li$^+$|O(DEE) coordination number (CN), and 2) the Li$^+$|N distance (considering a specific MOF-linker). We use the following definition of CN:

$$CN = \sum_{i=1}^{N} \frac{1-\left(\dfrac{r_i}{r_0}\right)^p}{1-\left(\dfrac{r_i}{r_0}\right)^q}$$

where $p = 6$, $q = 12$, r_i is the distance between Li$^+$ and the i-th coordinating atom (in this case the Li$^+$ and oxygen of DEE), and $r_0 = 3.07$Å is the cut-off radius that defines atoms as inside or outside of the first solvation sphere.

The Metadynamics biases were constructed as follows: The widths were 0.05 and 0.05 for the CN and the distance respectively, with a height of 0.02 kcal/mol and a depositing frequency 200fs. Each simulation was run for at least 78ns and we monitored convergence by ensuring that the collective variables were ballistic. All simulations were performed using the Colvars module in LAMMPS.

Supplementary Tables

Table S1. Computed bulk diethyl ether (DEE) density and entropy at 298K. The DEE

OPLS-AA parameters were described by Lennard-Jones (LJ) potential: $E_{LJ} = 4\varepsilon\left[\left(\frac{\sigma}{r}\right)^{12} - \left(\frac{\sigma}{r}\right)^{6}\right]$.

To well reproduce the DEE density and entropy properties, the LJ epsilon (ε) and sigma (σ)
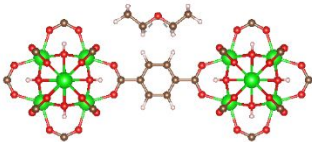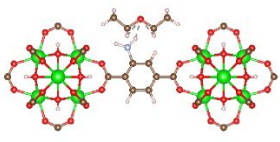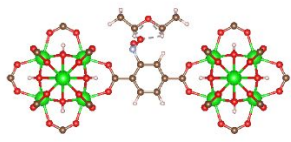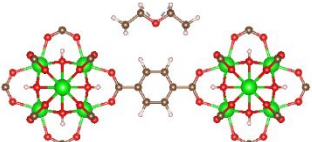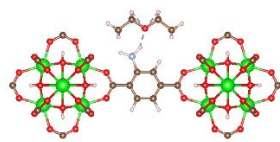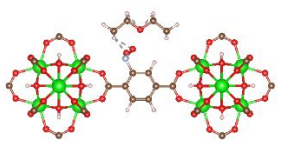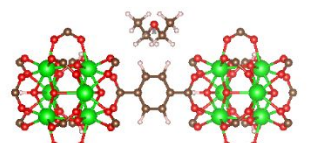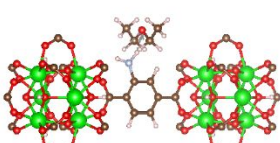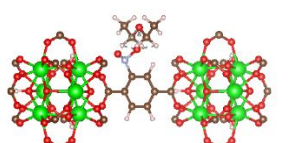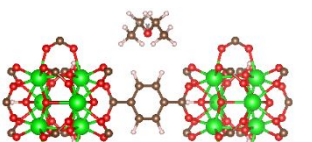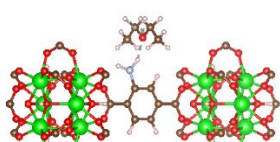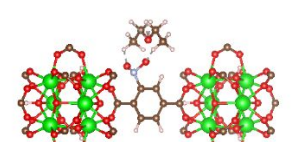
values were slightly adjusted by scaling factors (λ_ε and λ_σ), which resulted in an adjusted LJ

potential: $E_{LJ\_adjusted} = 4\varepsilon\lambda_\varepsilon\left[\left(\frac{\sigma\lambda_\sigma}{r}\right)^{12} - \left(\frac{\sigma\lambda_\sigma}{r}\right)^{6}\right]$.   According to NIST, entropy of the liquid

DEE at 298K is 253 J/mol_K[18] and the density at 293K is 0.714 g/cm³.[24]

epsilon scaling factor λ_ε	sigma scaling factor λ_σ	Density (g/cm³)	Entropy (J/mol_K)
1	1	0.701	224.6
1	0.9	0.749	233.5
1	0.85	0.750	241.8
0.975	0.8	0.640	256.9
0.95	0.875	0.700	245.1
0.95	0.85	0.707	248.4
0.95	0.825	0.667	252.9
0.9	1	0.660	231.3
0.9	0.9	0.685	245.7
0.9	0.885	0.674	246.9
0.9	0.85	0.659	252.1
0.8	1	0.599	243.1
0.8	0.9	0.535	262.8

Table S2. Computed MOF|DEE interaction energies. 4 MOF|DEE configurations were

calculated for each MOF linker. The interaction energies between the MOF and DEE were

computed every 0.5Å MOF-DEE distances and the binding energy (BE) shown below.

	UiO-66 | 1DEE	UiO-66-NH$_2$ | 1DEE	UiO-66-NO$_2$ | 1DEE
#1	BE=-0.23 eV	BE=-0.04 eV	BE=-0.08 eV
#2	BE=-0.38 eV	BE=-0.18 eV	BE=-0.02 eV
#3	BE= -0.15 eV	BE= -0.03 eV	BE= -0.08 eV
#4	BE= -0.24 kcal/mol	BE= -0.24 eV	BE= -0.02 eV

Table S3. Comparison between QM and forcefield (FF) energies. An energy shift of -

0.38eV, -2.27eV, and -3.53eV was applied in the parameterization process for UiO-66, UiO-

66-NH$_2$, and UiO-66-NO$_2$, respectively.

MOFs	QM|FF Energies and optimized parameters
UiO-66	QM|FF Energies:

Optimized parameters:

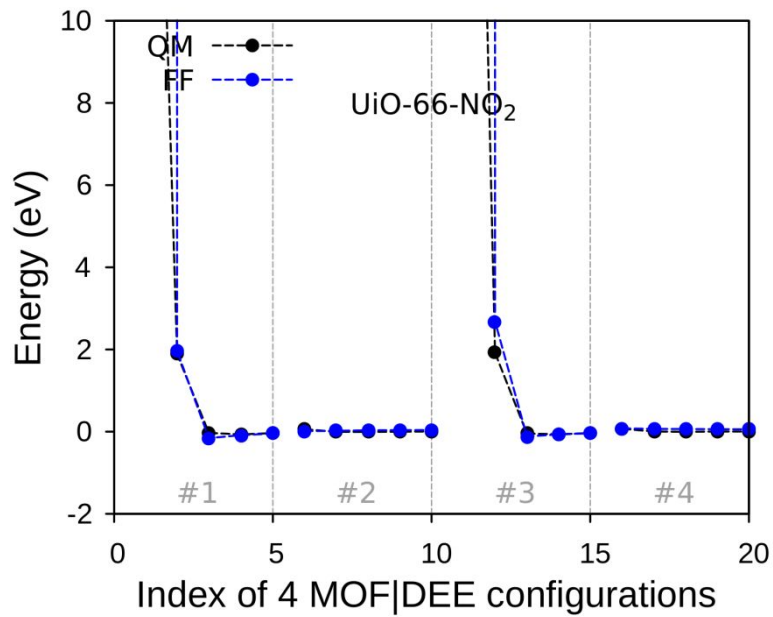| Atom of BDC linker	Atom of DEE	Lennard-Jones epsilon (eV)	Lennard-Jones sigma (Å)
C of BDC	C of CH$_3$	1.593E-03	3.433
C of BDC	C of CH$_2$	2.584E-03	3.289
C of BDC	O	3.470E-03	3.053
C of BDC	H of CH$_3$	8.303E-04	3.043
C of BDC	H of CH$_2$	2.180E-03	2.798
H of BDC	C of CH$_3$	1.334E-03	2.928
H of BDC	C of CH$_2$	1.950E-03	2.813
H of BDC	O	2.439E-03	2.595
H of BDC	H of CH$_3$	7.827E-04	2.511
H of BDC	H of CH$_2$	1.503E-03	2.353

UiO-66-NH$_2$	**QM|FF Energies:**
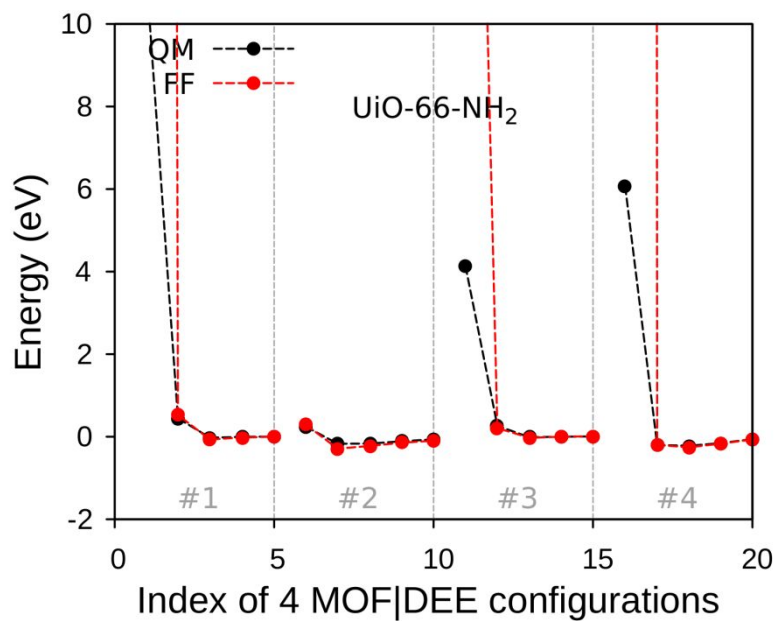
Optimized parameters:

| Atom of functionalized BDC linker	Atom of DEE	Lennard-Jones epsilon (eV)	Lennard-Jones sigma (Å)
N of BDC-NH$_2$	C of CH$_3$	6.774E-04	3.558
N of BDC-NH$_2$	C of CH$_2$	1.720E-03	3.244
N of BDC-NH$_2$	O	1.415E-03	3.162
N of BDC-NH$_2$	H of CH$_3$	2.255E-04	3.267
N of BDC-NH$_2$	H of CH$_2$	1.902E-03	2.667
H of BDC-NH$_2$	C of CH$_3$	6.079E-05	3.703
H of BDC-NH$_2$	C of CH$_2$	9.775E-04	2.897
H of BDC-NH$_2$	O	9.947E-05	2.950
H of BDC-NH$_2$	H of CH$_3$	8.667E-12	9.406
H of BDC-NH$_2$	H of CH$_2$	2.119E-03	2.186

UiO-66-NO$_2$	QM|FF Energies:

Optimized parameters:

| Atom of functionalized BDC linker	Atom of DEE	Lennard-Jones epsilon (eV)	Lennard-Jones sigma (Å)
N of BDC-NO$_2$	C of CH$_3$	2.735E-03	3.131
N of BDC-NO$_2$	C of CH$_2$	2.085E-03	3.209
N of BDC-NO$_2$	O	4.043E-03	2.870
N of BDC-NO$_2$	H of CH$_3$	1.884E-03	2.700
N of BDC-NO$_2$	H of CH$_2$	1.239E-03	2.803
O of BDC-NO$_2$	C of CH$_3$	2.442E-03	3.074
O of BDC-NO$_2$	C of CH$_2$	3.071E-04	3.731
O of BDC-NO$_2$	O	3.293E-03	2.837
O of BDC-NO$_2$	H of CH$_3$	1.806E-03	2.629
O of BDC-NO$_2$	H of CH$_2$	1.261E-08	5.763

Table S4. Transfer thermodynamics of DEE from the bulk liquid into the MOF at the

thermodynamic saturation limit.

MOF	Pressure (atm)	Averaged ΔA (kJ/mol)	Averaged ΔH (kJ/mol)	Averaged TΔS (kJ/mol)
UiO-66	>0.089	-12.5	-30.9	-18.2
UiO-66-NO$_2$	>0.00044	-15.4	-41.9	-26.3
UiO-66-NH$_2$	>0.0023	-14.7	-36.3	-21.5
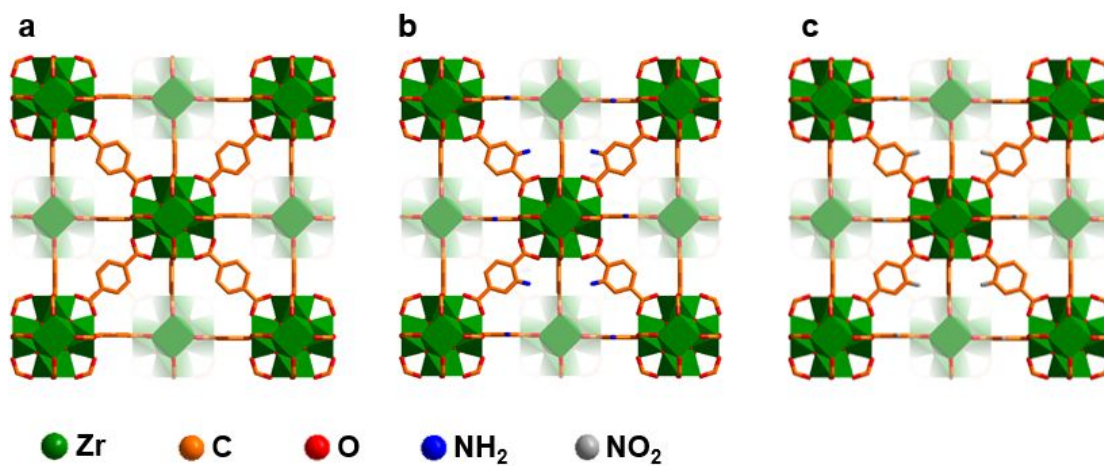
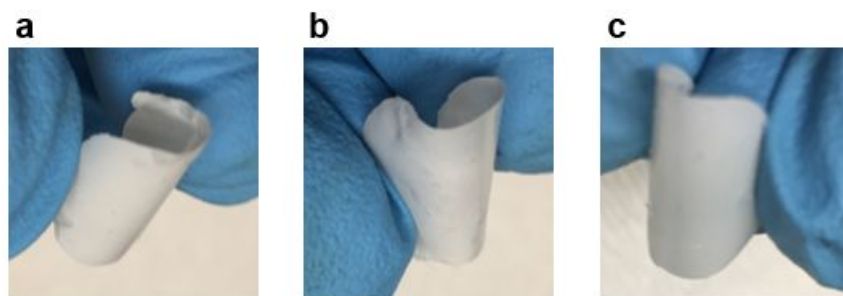**Figure S1.** Crystal structures of (a) UiO-66, (b) UiO-66-NH_2, (c) UiO-66-NO_2.
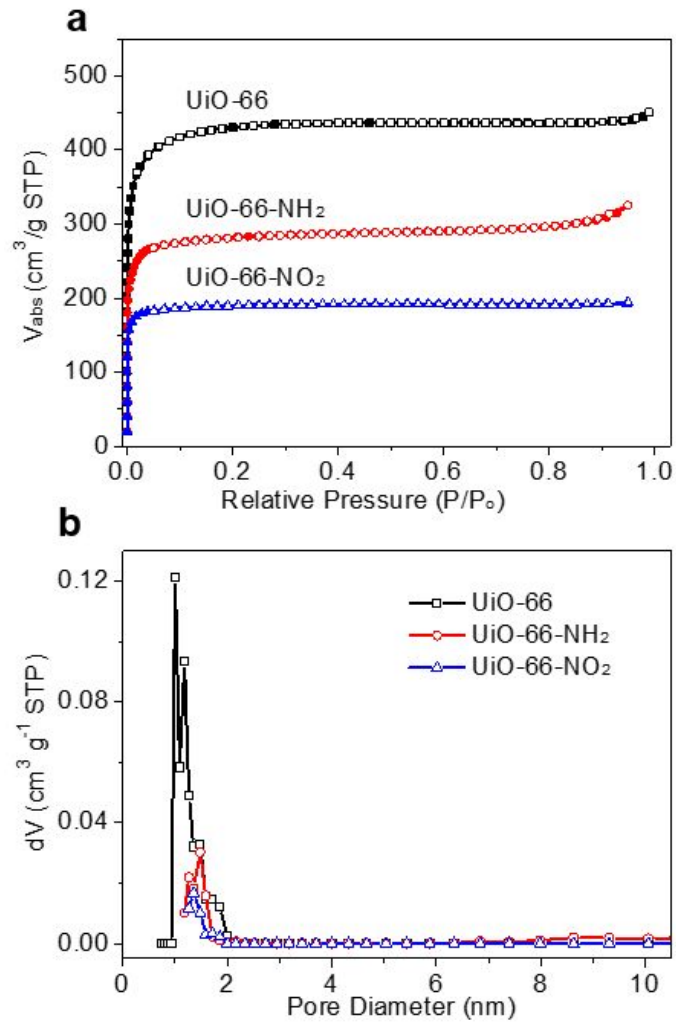
Figure S2. (a) N_2 sorption isotherms and (b) pore size distribution of UiO-66, UiO-66-NH$_2$,

and UiO-66-NO$_2$ with a BET specific surface area of 1300, 852, and 571 m^2 g^{-1}, respectively.
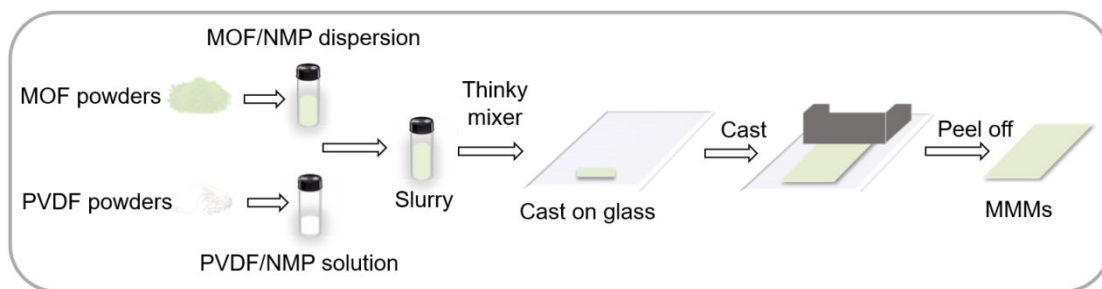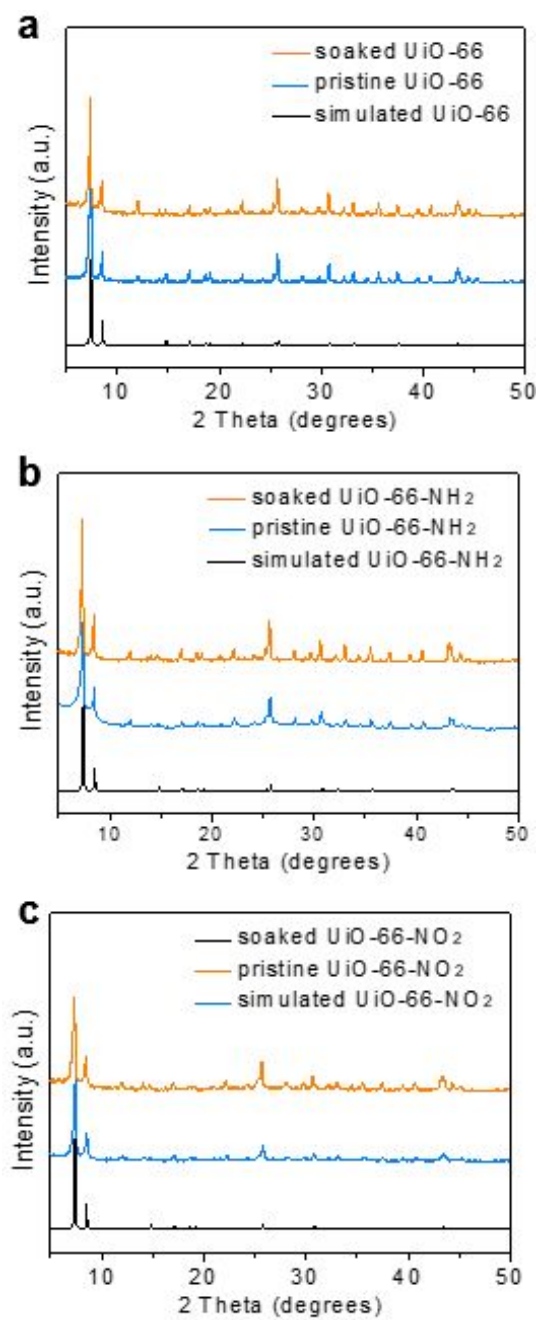
Figure S3. Schematic showing the fabrication process of free-standing MOF/polymer mixed-matrix membranes (MMMs).

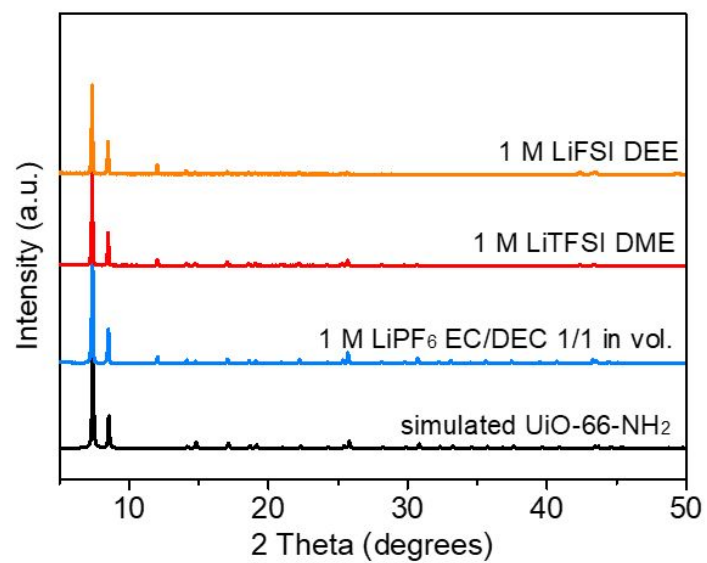**Figure S4.** Digital photograph of UiO-66-MMM.

Figure S5. Photographs of UiO-66-MMMs bending after soaking in (a) DEE, (b) 1,2 dimethoxyethane (DME), and (c) propylene carbonate (PC) over 7 days.
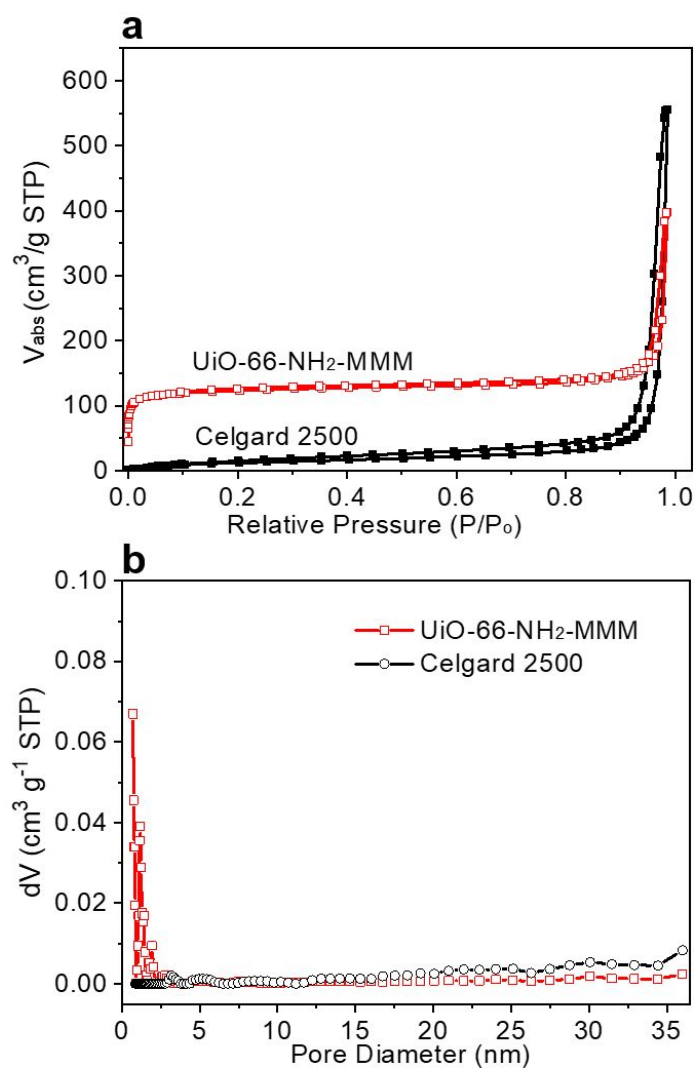
Figure S6. XRD patterns of (a) UiO-66, (b) UiO-66-NH$_2$, and (c) UiO-66-NO$_2$ before and after
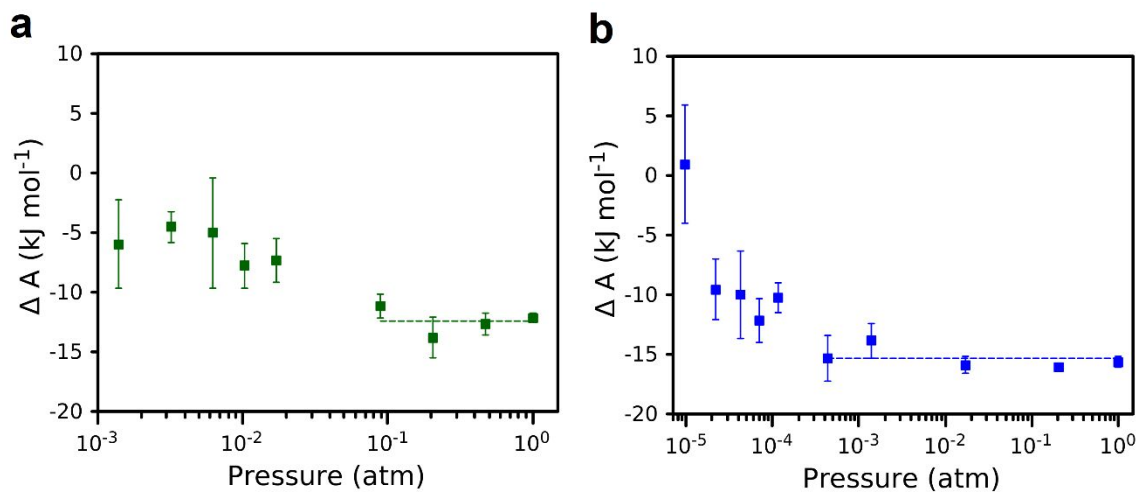
soaking in DME and DEE.

**Figure S7.** XRD patterns of UiO-66-NH$_2$ after soaking in different electrolytes overnight at

50°C, including 1 M LiPF$_6$ EC/DEC 1/1 in vol., 1 M LiTFSI DME and 1 M LiFSI DEE.

Figure S8. (a) N_2 sorption isotherms and (b) pore size distribution of UiO-66-NH$_2$-MMMs

and commercial Celgard 2500 membranes with a total pore volume of 0.616 and 0.858 cm^3 g$^-$

^{1}, respectively.

Figure S9. Helmholtz free energy difference for transferring a DEE molecule from the bulk liquid into (a) UiO-66 (green squares) and (b) UiO-66-NO$_2$ (blue squares) pores, at 298K. The uncertainty in our calculations (standard deviation) are given by the error bars. Dashed horizontal lines indicate the saturated thermodynamic limit.
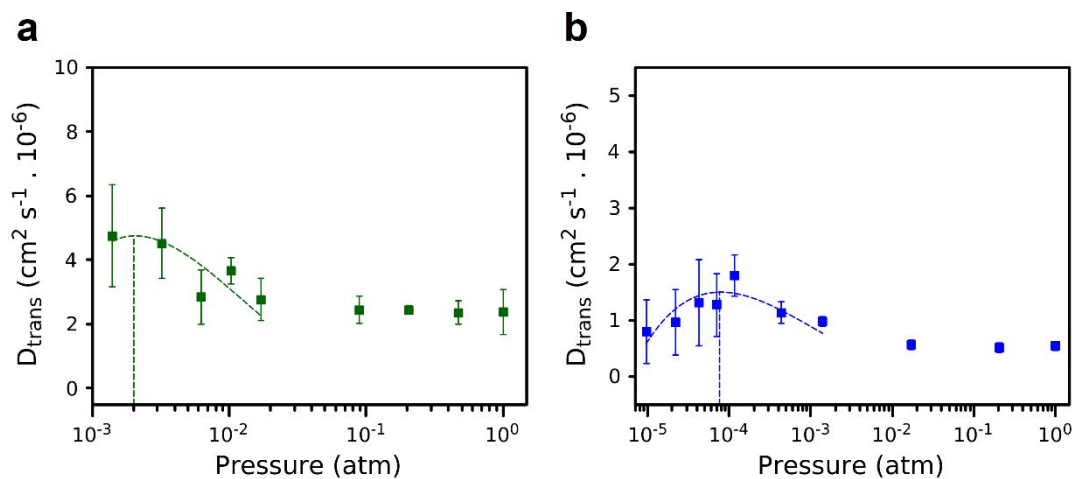
Figure S10. DEE translational diffusion coefficient (D_{trans}) in (a) UiO-66 (green squares) and (b) UiO-66-NO$_2$ (blue squares) at 298K. The uncertainty in our calculations (standard deviation) is given by the error bars. The turning points indicate the phase transition pressures.
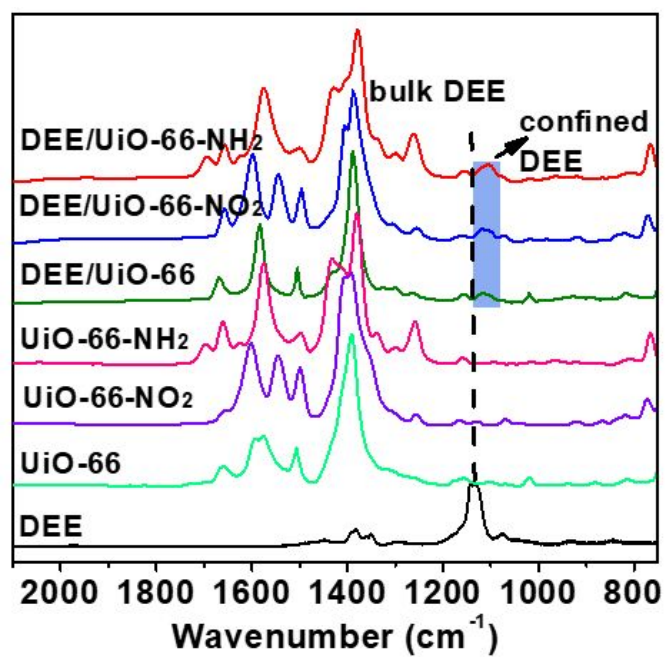
Figure S11. Experimental FTIR spectra of DEE, MOFs, and DEE-soaked MOFs.
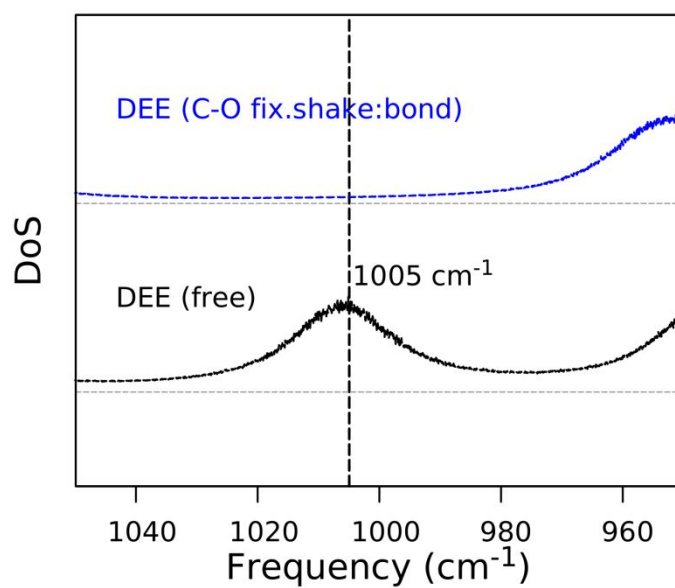
Figure S12. Vibrational density of states (i.e., spectral density) function of the bulk DEE, where we constraint the C-O bond stretch using the SHAKE[25] algorithm (top panel) and without constraints (bottom panel). We thus fingerprint the signature of the C-O stretching, which corresponds to an experimental frequency of ~1100 cm^{-1}.
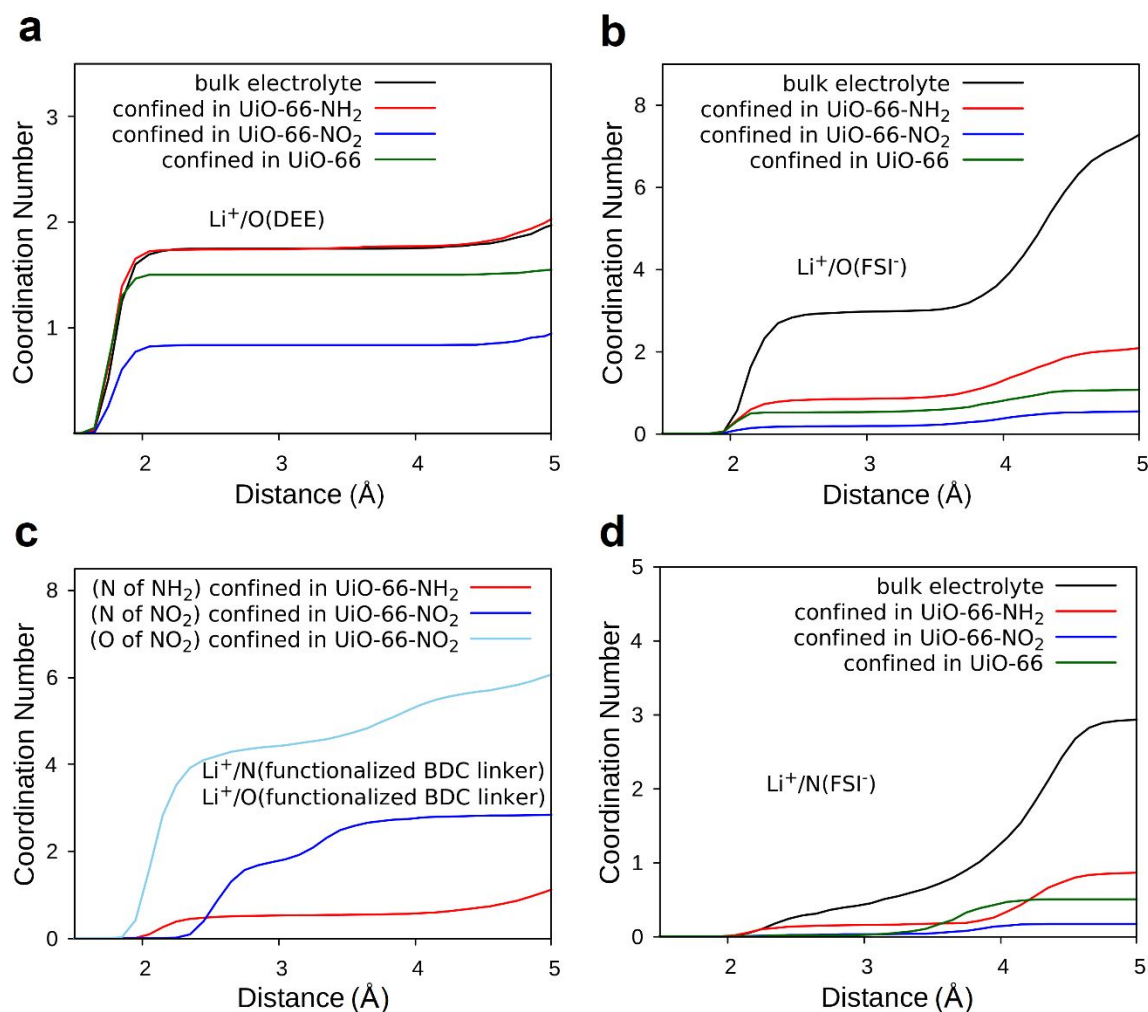
**Figure S13.** (a) Calculated coordination between the oxygen of DEE and Li$^+$ ions, for the bulk electrolyte (black), UiO-66-NH$_2$ (red), UiO-66-NO$_2$ (blue) and UiO-66 (green) from 298K equilibrium MD simulations. (b) Li$^+$-Oxygen (FSI$^-$) coordination number, in UiO-66, UiO-66-NH$_2$, UiO-66-NO$_2$, and the bulk electrolytes at 298K. (c) Li$^+$-Nitrogen|Oxygen (functionalized BDC linker) coordination number, in UiO-66-NH$_2$ and UiO-66-NO$_2$, at 298K. (d) Li$^+$-Nitrogen (FSI$^-$) coordination number, in UiO-66, UiO-66-NH$_2$, UiO-66-NO$_2$, and the bulk electrolytes at 298K.
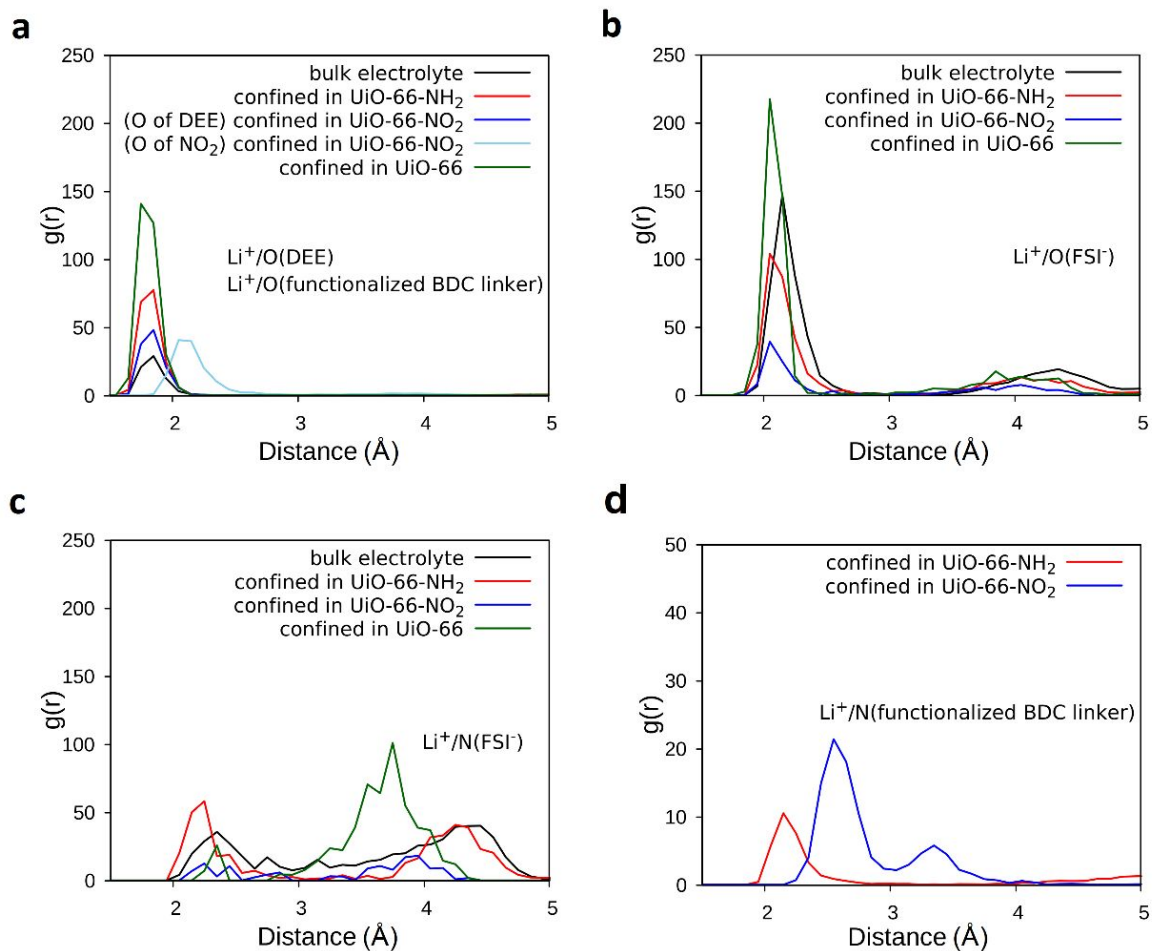
Figure S14. Radial distribution functions for (a) Oxygen (DEE and functionalized BDC linker), (b) Oxygen (FSI⁻), (c) Nitrogen (FSI⁻), and (d) Nitrogen (functionalized BDC linker) atoms coordinated with Li⁺ ion at 1atm, 298K.

LiFSI | DEE | UiO-66-NH₂   **LiFSI | DEE | UiO-66-NO₂**

LiFSI | DEE | UiO-66   **LiFSI | DEE**
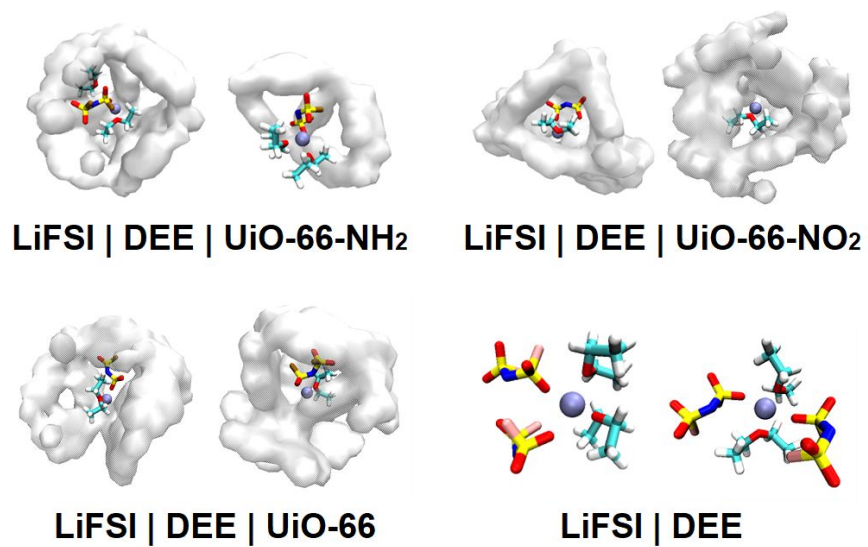
Figure S15. MD snapshots of the most representative electrolyte solvation structures inside

UiO-66-NH$_2$, UiO-66, and UiO-66-NO$_2$ and the structure in the bulk case at 298K.
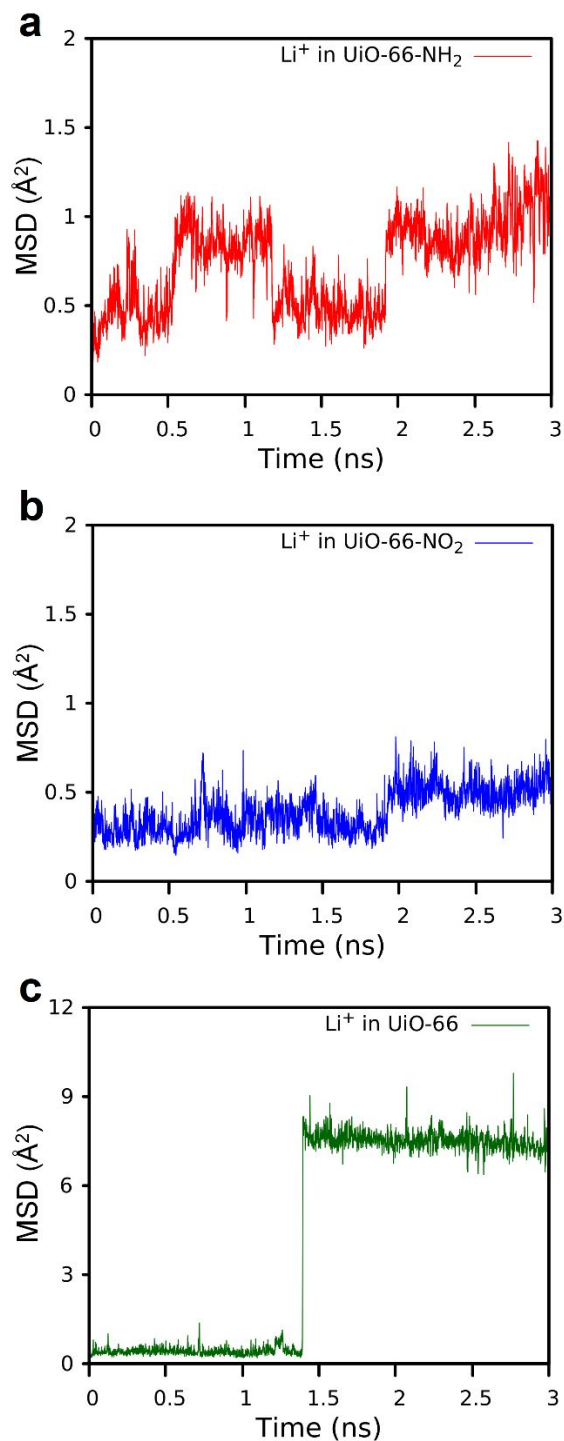
Figure S16. Li^+ ion transport in (a) UiO-66-NH$_2$, (b) UiO-66-NO$_2$, and (c) UiO-66 calculated by Mean Square Displacement (MSD). The MSD values were saved every 10 fs and plotted using the averaged values of every 100 data points (1ps) for clarify.
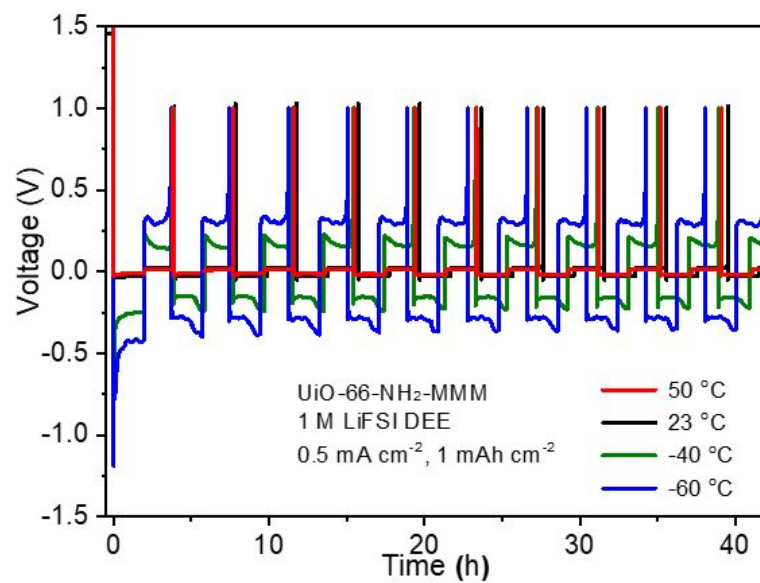
Figure S17. The wide-temperature testing of Li//Cu with UiO-66-NH$_2$-MMM trapped electrolyte system.
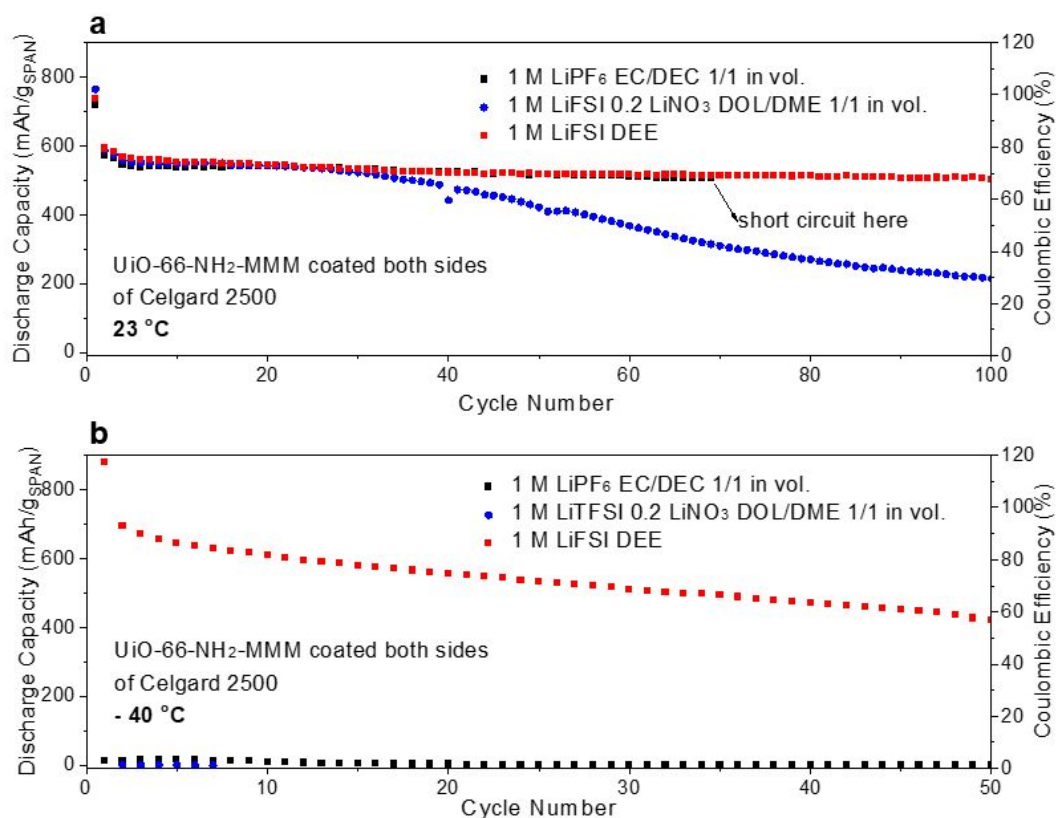
Figure S18. Long-term cycling testing of Li//SPAN coin cells at (a) 23 and (b) -40 °C based

on the MMMs trapped 1 M LiFSI DEE, and the common liquid electrolyte systems (e.g., 1 M

LiPF$_6$ EC/DEC 1/1 in vol., 1 M LiTFSI 0.2 LiNO$_3$ DOL/DME 1/1 in vol.) with the Celgard

membrane as the separator.

Video S1. Violability testing of DEE and common electrolyte solvents.

Video S2. Wettability testing of MMMs with different functionalized MOFs toward 1 M

LiFSI DEE.

Reference

1   Kaminski, G. A., Friesner, R. A., Tirado-Rives, J. & Jorgensen, W. L. Evaluation and Reparametrization of the OPLS-AA Force Field for Proteins via Comparison with Accurate Quantum Chemical Calculations on Peptides†. *J. Phys. Chem. B* **105**, 6474-6487 (2001).

2   Jorgensen, W. L., Maxwell, D. S. & Tirado-Rives, J. Development and Testing of the OPLS All-Atom Force Field on Conformational Energetics and Properties of Organic Liquids. *J. Am. Chem. Soc.* **118**, 11225-11236 (1996).

3   Plimpton, S. Fast Parallel Algorithms for Short-Range Molecular Dynamics. *Journal of Computational Physics* **117**, 1-19 (1995).

4   Ceriotti, M., Bussi, G. & Parrinello, M. Colored-Noise Thermostats à la Carte. *J. Chem. Theory Comput.* **6**, 1170-1180 (2010).

5   Ramji, R. & Pascal, T. 2PT post trajectory analysis code. doi:10.5281/ZENODO.7731073 (2023).

6   Pascal, T. A., Lin, S.-T. & Goddard III, W. A. Thermodynamics of liquids: standard molar entropies and heat capacities of common solvents from 2PT molecular dynamics.   **13**, 169-181 (2011).

7   Rappi, A. K., Casewit, C. J., Colwell, K. S., III, W. A. G. & Skid, W. M. UFF, a Full Periodic Table Force Field for Molecular Mechanics and Molecular Dynamics Simulations *J. Am. Chem. Soc.* **114**, 10024-10035 (1992).

8   Rappe, A. K. & Goddard III, W. A. Charge equilibration for molecular dynamics simulations. *Journal of Physical Chemistry* **95**, 3358-3363 (1991).

9   Boyd, P. G., Moosavi, S. M., Witman, M. & Smit, B. Force-Field Prediction of Materials Properties in Metal-Organic Frameworks. *J. Phys. Chem. Lett.* **8**, 357-363 (2017).

10   Wang, Q. & Tang, S. Energy storage analysis of R125 in UIO-66 and MOF-5 nanoparticles: A molecular simulation study. *Open Chemistry* **17**, 229-234 (2019).

11   Giannozzi, P. *et al.* QUANTUM ESPRESSO: a modular and open-source software project for quantum simulations of materials. *Journal of Physics: Condensed Matter* **21**, 395502 (2009).

12   Grimme, S., Antony, J., Ehrlich, S. & Krieg, H. A consistent and accurate ab initio parametrization of density functional dispersion correction (DFT-D) for the 94 elements H-Pu. *J. Chem. Phys.* **132**, 154104 (2010).

13   Martin, M. G. MCCCS Towhee: a tool for Monte Carlo molecular simulation. *Molecular Simulation* **39**, 1212-1222 (2013).

14   Cai, G. *et al.* Sub-nanometer confinement enables facile condensation of gas electrolyte for low-temperature batteries. *Nature Communications* **12** (2021).

15   Green, M. S. Markoff random processes and the statistical mechanics of time-dependent phenomena. II. Irreversible processes in fluids. *The Journal of chemical physics* **22**, 398-413 (1954).

16   Kubo, R., Yokota, M. & Nakajima, S. Statistical-mechanical theory of irreversible processes. II. Response to thermal disturbance. *Journal of the Physical Society of Japan* **12**, 1203-1211 (1957).

17   Lide, D. CRC Handbook of Chemistry and Physics 87 edition 2592 by pp.   (2006).

18   Counsell, J. F., Lee, D. A. & Martin, J. F. Thermodynamic properties of organic oxygen compounds. Part XXVI. Diethyl ether. *J. Chem. Soc. A*, 313-316 (1971).

19   Liu, H. *et al.* Ultrahigh coulombic efficiency electrolyte enables Li||SPAN batteries with superior cycling performance. *Materials Today* **42**, 17-28 (2021).

20   Laio, A. & Parrinello, M. Escaping free-energy minima. *Proc. Natl. Acad. Sci. U. S. A.* **99**, 12562-12566 (2002).

21   Barducci, A., Bonomi, M. & Parrinello, M. Metadynamics. *WIREs Computational Molecular Science* **1**, 826-843 (2011).

22   Ensing, B., De Vivo, M., Liu, Z., Moore, P. & Klein, M. L. Metadynamics as a Tool for Exploring Free Energy Landscapes of Chemical Reactions. *Accounts of Chemical Research* **39**, 73-81 (2006).

23   Barducci, A., Bussi, G. & Parrinello, M. Well-tempered metadynamics: a smoothly converging and tunable free-energy method. *Phys. Rev. Lett.* **100**, 020603 (2008).

24   Guard, U. S. C. *Chemical Hazards Response Information System (CHRIS) Hazardous Chemical Data* (Department of Transportation 1999).

25   Ryckaert, J.-P., Ciccotti, G. & Berendsen, H. J. C. Numerical integration of the cartesian equations of motion of a system with constraints: molecular dynamics of n-alkanes. *Journal of computational physics* **23**, 327-341 (1977).